Letter

High-temperature quantum anomalous Hall effect in buckled honeycomb antiferromagnets

Mohsen Hafez-Torbati [1,*] and Götz S. Uhrig [2,†]
[1]*Department of Physics, Shahid Beheshti University, 1983969411 Tehran, Iran*
[2]*Condensed Matter Theory, Department of Physics, TU Dortmund University, 44221 Dortmund, Germany*

(Received 28 October 2025; revised 27 January 2026; accepted 9 March 2026; published 6 April 2026)

We propose Néel antiferromagnetic (AF) Mott insulators with a buckled honeycomb structure as potential candidates to host a high-temperature AF Chern insulator (AFCI). Using a generalized Kondo lattice model, we show that the staggered potential induced by a perpendicular electric field due to the buckling can drive the AF Mott insulator to an AFCI phase. We address the temperature evolution of the Hall conductance and the chiral edge states. The quantization temperature T_q, below which the Hall conductance is quantized, depends essentially on the strength of the spin-orbit coupling and the hopping parameter, independent of the specific details of the model. The deviation of the Hall conductance from the quantized value e^2/h above T_q is found to be accompanied by a spectral broadening of the chiral edge states, reflecting a finite life-time, i.e., a decay. Using parameters typical for heavy transition-metal elements we predict that the AFCI can survive up to room temperature. We suggest $Sr_3CaOs_2O_9$ as a potential compound to realize a high-T AFCI phase.

DOI: 10.1103/nmxv-m2wf

Introduction. Due to its far-reaching potential applications in topological quantum computation and low-energy-consumption spintronic devices the Chern insulator (CI) state has attracted considerable attention in the past decade [1,2]. This has lead to the discovery of the CI in different classes of systems including thin films of magnetically doped topological insulators [3–5], thin films of the intrinsic magnetic topological insulator $MnBi_2Te_4$ [6–8], and moiré materials [9,10]. Despite this remarkable progress, the observation of the CI is limited to temperatures of only a few Kelvins, arising from the material's negligible charge gap or low magnetic transition temperature.

While the current realization of the CI is limited to ferromagnets, antiferromagnets are far more common and exhibit generally higher transition temperatures, reaching hundreds of Kelvins [11]. In addition, the AF ordering of strongly correlated electrons is known to be accompanied with a noticeable blue shift of the charge gap [12–15]. This is to be compared with the ferromagnetic ordering on the top and the bottom surfaces of $MnBi_2Te_4$ inducing almost no gap in the Dirac states [16–19]. Thus, there is compelling reason to search for a high-temperature CI in AF Mott materials.

A nonzero Chern number necessitates the time-reversal symmetry to be truly broken [20,21]. This is inherent in ferromagnets but not guaranteed in antiferromagnets. The effect of the time-reversal transformation on an AF state can be compensated by a lattice group operation. This composite antiunitary symmetry needs to be broken for the emergence of an AFCI, which is usually achieved by inducing a staggered potential between the spin-up and the spin-down sublattices [20–22]. The direction of the magnetization on the higher-energy (or the lower-energy) sublattice determines the clockwise or the counterclockwise propagation direction of the chiral edge states. The AFCI phase is already predicted in various systems [20–25]. For those involving heavy transition-metal elements a large charge gap is also reported [24,25]. However, an explicit study of whether the AFCI can persist up to high temperatures remains a crucial open question.

Here, we investigate the Néel AF transition-metal compounds possessing a buckled honeycomb structure, see Fig. 1(a). Using a generalized Kondo lattice model we confirm that a perpendicular electric field can drive the AF Mott insulating state to an AFCI phase. We address the temperature evolution of the Hall conductance and the chiral edge states. The quantization temperature T_q, below which the Hall conductance is quantized, shows generic behavior depending only on the spin-orbit coupling and the hopping parameter. The deviation of the Hall conductance from the quantized value e^2/h above T_q is accompanied by a spectral broadening of the chiral edge modes. For heavy transition-metal elements we estimate that T_q can reach room temperature. We propose $Sr_3CaOs_2O_9$ as a potential candidate to realize a high-T AFCI state.

Model Hamiltonian. The low-energy properties of transition-metal compounds are commonly described by the spin-$\mathcal{S}_{\text{tot}}$ Heisenberg model [26]

$$H = J \sum_{\langle i,j \rangle} \vec{\mathcal{S}}_i \cdot \vec{\mathcal{S}}_j + \cdots , \tag{1}$$

where $\langle i, j \rangle$ limits i and j to be nearest-neighbor (NN) and the dots stand for terms beyond the isotropic NN interaction. For the Néel AF order, the NN AF interaction ($J > 0$) is usually the dominant term.

For the buckled honeycomb structure, see Fig. 1(a) for a side view, applying a perpendicular electric field induces a potential difference between the spin-up and the spin-down sublattices. This induces a shift of charges between the two

*Contact author: m.hafeztorbati@gmail.com
†Contact author: goetz.uhrig@tu-dortmund.de

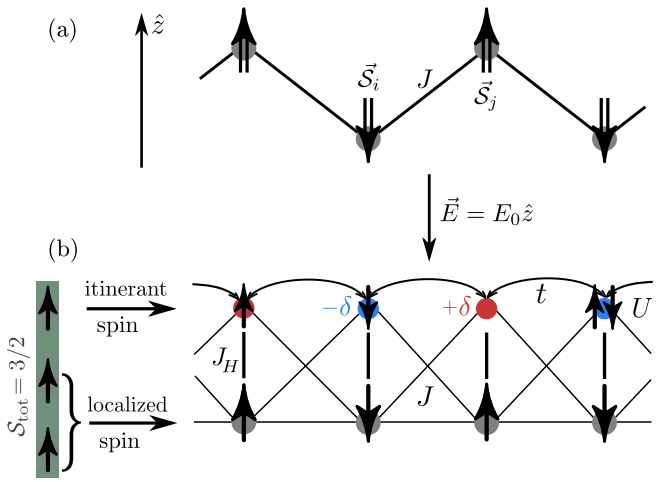

FIG. 1. (a) Side view of the spin-$\mathcal{S}_{\rm tot}$ Heisenberg model with the nearest-neighbor AF interaction J on the buckled honeycomb structure. In the presence of a perpendicular electric field $\vec{E} = E_0\hat{z}$ the system can effectively be described by the generalized Kondo lattice model (2) illustrated in (b) for the special case of $\mathcal{S}_{\rm tot} = 3/2$.

kinds of sites. The description of the system requires the Heisenberg model (1) to be extended by the charge degrees of freedom, and the multiorbital Hubbard model would be the natural choice. However, a reliable analysis of the topological properties of a strongly correlated multiorbital model at finite temperature is a too ambitious numerical challenge. For this reason, we follow the idea proposed in Ref. [14] which was successful in the description of different compounds [12,13]. We approximate the multiorbital Hubbard model by a generalized Kondo lattice model. This is well justified if the charge fluctuations, i.e., the number of holes or double occupancies, do not exceed one per site. The generalized Kondo lattice model is given by (cf. Fig. 1)

$$\begin{aligned} H = &+ t \sum_{\langle i,j\rangle} \sum_{\alpha} c^{\dagger}_{i\alpha} c_{j\alpha} - 2J_{\rm H} \sum_i \vec{s}_i \cdot \vec{S}_i + U \sum_i n_{i,\uparrow} n_{i,\downarrow} \\ &+ J \sum_{\langle i,j\rangle} (\vec{S}_i \cdot \vec{S}_j + \vec{S}_i \cdot \vec{s}_j + \vec{s}_i \cdot \vec{S}_j) \\ &+ \sum_i \sum_{\alpha} \delta_i n_{i\alpha} + {\rm i}\lambda_{\rm SO} \sum_{[i,j]} \sum_{\alpha\beta} \nu_{ij} c^{\dagger}_{i\alpha} \sigma^z_{\alpha\beta} c_{j\beta}, \end{aligned} \tag{2}$$

where $c^{\dagger}_{i\alpha}$ is the fermion creation operator at the site i with the z-component of the spin $\alpha = \uparrow$ or $\downarrow$. The first term is the NN hopping and the second term is the Hund coupling between the electron spin $\vec{s}_i$ and the localized spin $\vec{S}_i$ with the spin quantum number $S = \mathcal{S}_{\rm tot} - 1/2$. We treat one orbital as representative of the charge motion, while the others represent the localized spin. We emphasize that the Kondo lattice approximation in Eq. (2) does not mean that we distinguish between the different orbitals of the same shape. The itinerant orbital stands as a *representative* for all the orbitals [12–14]. This restricts the possible amount of charge transfer between the higher- and the lower-energy sublattices. However, it is very well justified for the values of δ accessible via realistic strengths of electric fields, see below and also the ionicity discussed in the Supplemental Material [27].

The third term in Eq. (2) is the Hubbard interaction with $n_{i\alpha} := c^{\dagger}_{i\alpha} c_{i\alpha}$, and the fourth term is the Heisenberg interaction between the NN spins. We always count the Heisenberg interaction on each lattice bond only once. The fifth term is the staggered sublattice potential giving the onsite energies $+\delta$ and $-\delta$ to the two sublattices of the honeycomb structure. Figure 1(b) illustrates these different terms for the special case of $\mathcal{S}_{\rm tot} = 3/2$.

The last term in Eq. (2) is included to account for the effect of the spin-orbit coupling. It is exactly the Kane-Mele term [30]. The notation $[i, j]$ restricts i and j to be next-nearest neighbor, σ^z stands for the Pauli matrix, and $\nu_{ij} = 2/\sqrt{3}(\hat{d}_1 \times \hat{d}_2)_z = \pm 1$ where $\hat{d}_1$ and $\hat{d}_2$ are the unit vectors along the two bonds the electron traverses from site j to site i. We add a chemical potential $\mu = U/2$ to the Hamiltonian (2) to satisfy the half-filling condition.

We always focus on large values of U and $J_{\rm H}$ corresponding to the Mott regime and fix the Heisenberg interaction in Eq. (2) to $J = 4t^2/\Delta_0$ with $\Delta_0 := U + 2SJ_{\rm H}$, called the bare Mott gap. This guarantees the Heisenberg model (1) as the low-energy effective model of the Hamiltonian (2) for $\delta = 0$, apart from some weak anisotropic interactions originating from the spin-orbit coupling $\lambda_{\rm SO}$. The Hamiltonian (2) generalizes the purely spin model (1) allowing for the study of the charge fluctuations induced by a perpendicular electric field.

The number of methods which allow for a reliable investigation of the topological properties of the strongly correlated Hamiltonian (2) at finite temperature are rare. We employ the dynamical mean-field theory (DMFT) [31] as an established method for strongly correlated systems and use the exact diagonalization (ED) as the impurity solver [31,32]. We specifically use the real-space realization of the DMFT [33–35] providing access to the bulk and the edge properties on equal footing [36]. The lattice model is mapped to a set of effective Anderson-Kondo impurity models, which treat the localized spin quantum mechanically [12,13]. The method takes the local charge and spin quantum fluctuations fully into account. The local quantum fluctuations leading to a frequency-dependent self-energy are essential for the description of the paramagnetic Mott insulator at finite temperature. The nonlocal Heisenberg interactions are replaced by an effective AF field via a mean-field decoupling [37]. The strength of the effective AF field is determined self-consistently during the DMFT loop [12,13]. Further technical details can be found in the Supplemental Material [27]. Previous studies of similar interacting topological models by different methods indicate only minor effects to the phase boundaries due to the nonlocal quantum fluctuations, neglected in our investigation [38–42]. We will compare the results for the different number of bath sites in the ED calculations.

The Hall conductance for an interacting model at finite temperature can be computed [43–45] from the Matsubara Green's function $\boldsymbol{G}_{\alpha}({\rm i}\omega_n, \vec{k}) = [{\rm i}\omega_n \mathbb{1} - \boldsymbol{\mathcal{H}}^{(0)}_{\alpha}(\vec{k}) - \boldsymbol{\Sigma}_{\alpha}({\rm i}\omega_n)]^{-1}$ as

$$\begin{aligned} \sigma_{xy} = \frac{e^2}{h} \frac{T}{12\pi} \epsilon_{\mu\nu\rho} {\rm Im} \Bigg[\sum_{\alpha} \sum_{n} \int {\rm d}\vec{k} {\rm Tr} \big[\boldsymbol{G}_{\alpha} \partial_{\mu} \boldsymbol{G}^{-1}_{\alpha} \\ \times \boldsymbol{G}_{\alpha} \partial_{\nu} \boldsymbol{G}^{-1}_{\alpha} \boldsymbol{G}_{\alpha} \partial_{\rho} \boldsymbol{G}^{-1}_{\alpha} \big] \Bigg], \end{aligned} \tag{3}$$

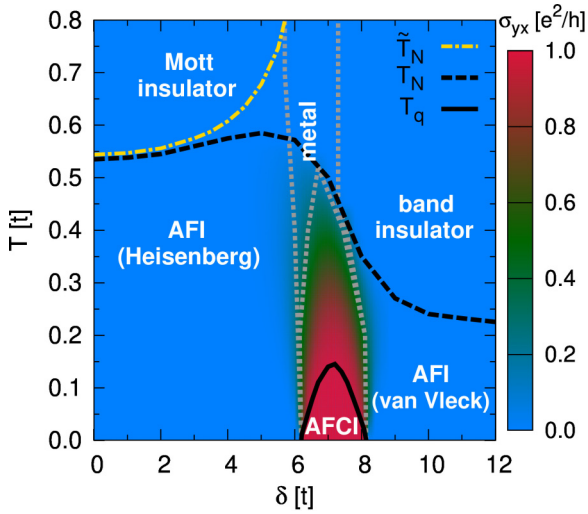

FIG. 2. Phase diagram of temperature versus the alternating sublattice potential controlled by a perpendicular electric field. The colormap represents the value of the Hall conductance $\sigma_{yx} = -\sigma_{xy}$ given by Eq. (3). The Néel temperature T_N and the crossover quantization temperature T_q are specified. The Hall conductance takes the quantized value e^2/h with an error less than %1 below T_q, characterizing the antiferromagnetic Chern insulator (AFCI). The gray dotted lines separate the metallic region from the insulating regions. The metallic region shrinks rapidly to the two quantum critical points as $T \to 0$. The mean-field Néel temperature $\tilde{T}_N$ of the effective low-energy spin model valid for small values of δ, see the main text, is also included. The results are for the model parameters $S = 1/2$, $U = 12t$, $J_H = 0.2U$, $J = 4t^2/\Delta_0 = 0.2\bar{7}t$, and $\lambda_{SO} = 0.2t$. We recall that the localized spin $S = 1/2$ in Eq. (2) corresponds to the total spin $\mathcal{S}_{tot} = S + 1/2 = 1$ in Eq. (1). The number of bath sites $n_b = 5$ is used in the ED impurity solver.

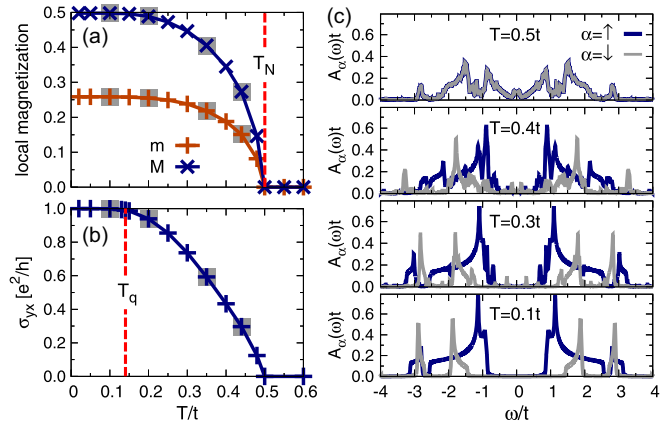

FIG. 3. (a) Local magnetizations $m = |\langle s_i^z \rangle|$ and $M = |\langle S_i^z \rangle|$ and (b) the Hall conductance versus T. The Néel temperature T_N and the crossover quantization temperature T_q are specified. (c) Local spectral function averaged over the two sites in the unit cell for the spin component α at different temperatures. The results correspond to the solution with the magnetization on the higher-energy sublattice pointing in the positive z direction. The results are for $S = 1/2$, $U = 12t$, $J_H = 0.2U$, $J = 4t^2/\Delta_0 = 0.2\bar{7}t$, $\lambda_{SO} = 0.2t$, and $\delta = 7t$. The data are for the number of bath sites $n_b = 6$ except for the filled gray squares at selective temperatures in (a) and (b) which are for $n_b = 7$.

where $\boldsymbol{\mathcal{H}}_\alpha^{(0)}(\vec{k})$ denotes the Bloch Hamiltonian matrix, $\boldsymbol{G}_\alpha \equiv \boldsymbol{G}_\alpha(i\omega_n, \vec{k})$, $\epsilon_{\mu\nu\rho}$ is the totally antisymmetric tensor, and summations are implied over the indices μ, ν, and ρ, each of which runs over $i\omega_n$, k_x, and k_y [27].

The momentum-resolved spectral function is accessed using the real-frequency Green's function

$$A_{\alpha,\vec{d}}(\omega, \vec{k}) = -\frac{1}{\pi}\mathrm{Im}[\boldsymbol{G}_\alpha(\omega + i\eta, \vec{k})]_{\vec{d},\vec{d}}, \tag{4}$$

where $\vec{d}$ specifies a lattice site in the unit cell. The broadening factor $\eta = 0.01t$ is used in the calculations. The local spectral function $A_{\alpha,\vec{d}}(\omega)$ is computed by integrating over the momentum with the appropriate prefactor. The spectral sum rule is always satisfied with an error less than 10^{-3} in all the results that we present.

Phase diagram. Figure 2 represents the phase diagram of temperature versus the alternating sublattice potential for the model parameters $S = 1/2$, $U = 12t$, $J_H = 0.2U$, $J = 4t^2/\Delta_0 = 0.2\bar{7}t$, and $\lambda_{SO} = 0.2t$. Note that the localized spin $S = 1/2$ in Eq. (2) corresponds to the total spin $\mathcal{S}_{tot} = 1$ in Eq. (1), see Fig. 1. The number of bath sites $n_b = 5$ is used in the ED. The colormap displays the value of the Hall conductance $\sigma_{yx} = -\sigma_{xy}$. The Néel temperature T_N and the crossover quantization temperature T_q are specified. The Hall conductance acquires the quantized value e^2/h with an error less than %1 below T_q, characterizing the AFCI. The gray dotted lines separate the metallic region from the insulating regions. The metallic region shrinks rapidly to the two quantum critical points as $T \to 0$. For small values of δ the system is a paramagnetic Mott insulator at high and an AFI at low T, which is the well-known physics of the Heisenberg model [46]. Upon increasing δ, the Néel temperature first increases. This is due to the increase in the effective Heisenberg interaction $J_{eff} = 4t^2\Delta_0/(\Delta_0^2 - 4\delta^2)$ between the *itinerant* spins. The mean-field Néel temperature $\tilde{T}_N$ of the effective low-energy spin model [27] nicely describes the Néel temperature T_N of the generalized Kondo lattice model up to $\delta \simeq 3t$. We attribute the small deviation to the contributions beyond the second-order perturbation theory used in the derivation of the effective spin model. For $\delta \gtrsim 5t$ the charge fluctuations start to play a qualitative role in the low-energy physics causing a drop in T_N. This behavior is reminiscent of the Néel temperature of the Hubbard model as the Hubbard interaction is reduced to lower values than in the Mott regime [47]. For large values of δ the lower-energy sublattice is almost doubly occupied and the higher-energy sublattice is almost empty of electrons. The itinerant electrons show a very weak local magnetization due to the van Vleck mechanism [27,48]. Thus, the itinerant electrons are in the band insulator phase above T_N.

The intermediate values of δ are of particular interest because the Hall conductance becomes nonzero and approaches the quantized value e^2/h as the temperature is lowered. For $\delta = 7t$ we plot the local magnetizations $m = |\langle s_i^z \rangle|$ and $M = |\langle S_i^z \rangle|$ in Fig. 3(a) and the Hall conductance versus T in Fig. 3(b). Figure 3(c) represents the local spectral function averaged over the two sites in the unit cell for the spin component α near the Fermi energy $\omega = 0$ at different temperatures. The finite spectral weight developing at the Fermi energy at

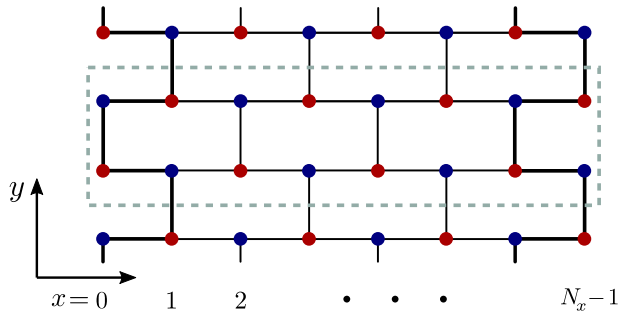

FIG. 4. The brick wall representation of the honeycomb structure with the open boundary condition in x and the periodic boundary condition in y direction. The different sites in the x direction are labeled from 0 to $N_x - 1$. The dashed box specifies the unit cell.

the paramagnetic high temperatures signals a metallic state. An intermediate metallic phase separating the band and the Mott insulators is already reported for the ionic Hubbard model [49,50]. Our results suggest that such a metallic phase appears also in multiorbital systems at paramagnetic high temperatures. At low temperatures, the system is expected to be an insulator [51–53].

The data in Fig. 3 are for $n_b = 6$ bath sites except for the filled gray squares at selective temperatures in Figs. 3(a) and 3(b), which are for $n_b = 7$. The results for $n_b = 5$, not included in the figure, also nicely match the results for $n_b = 6$ and 7. This corroborates the accuracy of the results.

Temperature evolution of chiral edge states. The quantized Hall conductance at intermediate values of δ in Fig. 2 is expected to support chiral edge states. The direction of magnetization on the higher-energy (or the lower energy) sublattice determines the clockwise or counterclockwise propagation direction of chiral edge states. We focus on the solution with the magnetization on the higher-energy sublattice pointing in the positive z direction. The other solution can be accessed using the time-reversal transformation.

To investigate the presence and the temperature evolution of the chiral edge states we consider a cylindrical geometry with open boundary condition in the x direction and edges of type armchair. The honeycomb structure is treated as a brick wall labeling the lattice sites in the x direction from 0 to $N_x - 1$, as illustrated in Fig. 4. At each x, there are two nonequivalent lattice sites in the y direction. We consider $N_x = 80$.

The momentum-resolved spectral function $A_{\uparrow,x=0}(\omega, k_y)$, averaged over the two nonequivalent lattice sites in the y direction, is plotted in Fig. 5(a) for the same model parameters as in Fig. 3. The results are for the topological spin component $\alpha = \uparrow$. The spin component $\alpha = \downarrow$ has no contribution to the quantized Hall conductance at low-T in Fig. 3(b) and we find it to be gapped in the bulk and at the edges. The chiral edge state in Fig. 5(a) at $T = 0.1t$ quickly disappears as the bulk is approached. This can be seen from the momentum-integrated spectral function $A_{\uparrow,x}(\omega)$ given for different values of x in Fig. 5(b). The temperature evolution of the momentum-resolved spectral function in Fig. 5(a) indicates a spectral broadening as the temperature is increased above $T \sim 0.2t$. This reflects a finite lifetime, i.e., a decay, of the chiral edge state and is in accord with the deviation of the Hall conductance from the quantized value e^2/h above T_q in Fig. 3(b).

Quantization temperature. Up to now, our study has been limited only to particular model parameters. Nevertheless, the AFCI always appears when the sublattice potential difference 2δ is of the same order as the bare Mott gap $\Delta_0 = U + 2SJ_H$, independent of the details of the model. The quantization temperature T_q also indicates generic behavior. To demonstrate this, we plot T_q versus the spin-orbit coupling in Fig. 6 for different sets of model parameters. In each case, the optimal value of δ is chosen such that the system is in the middle of the AFCI phase, see Fig. 2 for $\delta = 7.2t$ used in the last set of parameters. The Heisenberg interaction is always fixed to $J = 4t^2/\Delta_0$.

Interestingly, despite the very different model parameters used in Fig. 6 one can hardly see any change in T_q. The quantization temperature is solely determined by the spin-orbit coupling and the hopping parameter. T_q increases linearly with λ_{SO} and saturates for large values of λ_{SO}. Although the spin-orbit coupling is highly compound-specific, one usually expect $\lambda_{SO} < 0.15t$. In this region, the data can nicely be described by the linear fit $T_q = 0.92\lambda_{SO} - 0.003t$ shown in Fig. 6 as a black dashed line. This relation allows us to

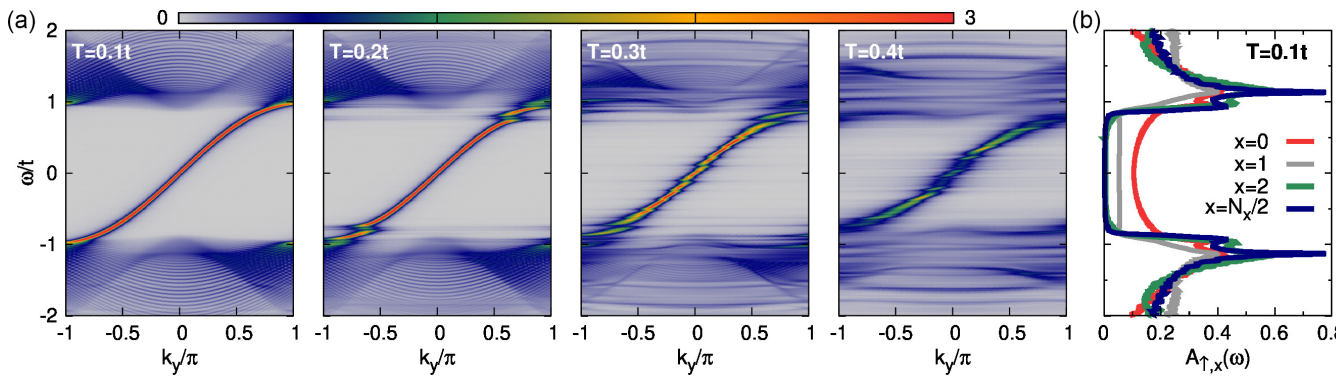

FIG. 5. (a) The momentum-resolved spectral function $A_{\alpha,x}(\omega, k_y)$ for the topological spin component $\alpha = \uparrow$ at the edge $x = 0$ at different temperatures. (b) Local spectral function $A_{\uparrow,x}(\omega)$ for $T = 0.1t$ at different x. The results are for the same model parameters as in Fig. 3. A cylindrical geometry as illustrated in Fig. 4 with $N_x = 80$ is used. The data are for $n_b = 6$ bath sites in the ED impurity solver.

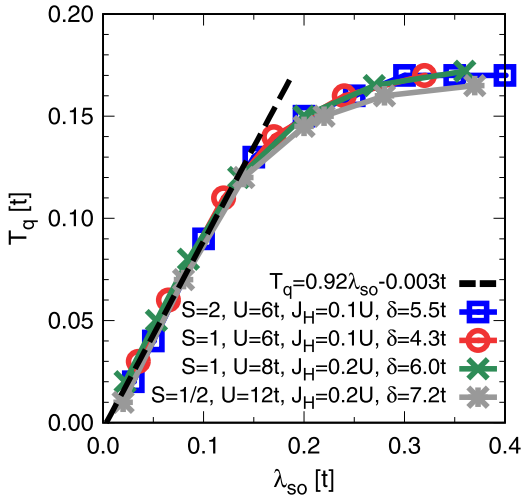

FIG. 6. Quantization temperature of the Hall conductance vs the spin-orbit coupling for different sets of model parameters. The Heisenberg interaction is always fixed to $J = 4t^2/\Delta_0$. In each case, the optimal value of δ is chosen such that the system is in the middle of the AFCI phase. The results are for the number of bath sites $n_b = 5$. The dashed line represents a linear fit to the data for $\lambda_{SO} < 0.15t$.

estimate the scale of the quantization temperature based on the knowledge of the spin-orbit coupling and the hopping parameter.

The precise determination of the strength of the spin-orbit coupling λ_{SO} in a material is challenging. However, it is usually estimated to be of the order of a few meV for $3d$, around 15 meV for $4d$, and around 40 meV for $5d$ transition-metal elements [54]. Note that the numbers refer to the Kane-Mele-type of the spin-orbit coupling. For comparison, the precise value of λ_{SO} for silicene, germanene, and stanene are computed to be 0.77, 8.9, and 12 meV, respectively [55]. Assuming $t \sim 200$ meV for $3d$ transition-metal compounds one finds that it is possible to realize the AFCI in these materials although with the small quantization temperature $T_q \sim 10$ K. This estimate nicely agrees with first-principles calculations predicting the AFCI in CrO with a small charge gap of about 1 meV at zero temperature [22]. For the more extended $4d$ orbital with the typical hopping parameter $t \sim 400$ meV we find $T_q \sim 100$ K. Assuming $t \sim 700$ meV for $5d$ materials, our results unveil the possible realization of the AFCI at room temperature.

Conclusion. We propose the strongly correlated AF materials with a buckled honeycomb structure as potential candidates to realize a hight-T CI phase. The system can be driven from the AF Mott insulating state to the AFCI phase by applying a perpendicular electric field, which allows to induce and fine-tune a sublattice potential difference. The AFCI emerges when the sublattice potential difference reaches the same size as the Mott gap. The experimentally accessible electric field of 0.5 V/Å [56–58] can induce a sublattice potential difference of a few eV in a buckling height of a few angstroms. Since the Mott gap and the buckling height can also be effectively controlled by pressure, we believe the AFCI state is realistically within reach.

Compounds Ba_2NiTeO_6 and $Sr_3CaOs_2O_9$ are known buckled honeycomb antiferromagnets with the buckling heights of 5.3 Å [59,60] and 3.3 Å [61], respectively. The latter compound shows a Néel AF order with the high Néel temperature $T_N \sim 385$ K and is a promising candidate to host a high-T AFCI. It should be noted that $Sr_3CaOs_2O_9$ is not anisotropic enough to be considered effectively two-dimensional and thin-film growth would be needed. It is also conceivable to strain-engineer the films to enhance the in-plane and further suppress the out-of-plane couplings to put the system closer to the two-dimensional limit. Growing [111]-oriented bilayers of perovskite heavy transition-metal oxides is another route to a buckled honeycomb antiferromagnet [62] and a high-T AFCI state. The possible realization of an AFCI in [111]-oriented perovskite bilayers has been previously predicted through studies of static exchange AF fields and first-principles calculations at zero temperature [63]. Our analysis going beyond static mean-field approaches and addressing the topological properties at finite temperatures explicitly unveils that AF Mott insulators can host a quantum anomalous Hall effect that can persist up to high temperatures.

Data availability. The data that support the findings of this article are not publicly available upon publication because it is not technically feasible and/or the cost of preparing, depositing, and hosting the data would be prohibitive within the terms of this research project. The data are available from the authors upon reasonable request.

[1] C.-Z. Chang, C.-X. Liu, and A. H. MacDonald, *Colloquium*: Quantum anomalous Hall effect, Rev. Mod. Phys. **95**, 011002 (2023).

[2] Y. Tokura, K. Yasuda, and A. Tsukazaki, Magnetic topological insulators, Nat. Rev. Phys. **1**, 126 (2019).

[3] C.-Z. Chang, J. Zhang, X. Feng, J. Shen, Z. Zhang, M. Guo, K. Li, Y. Ou, P. Wei, L.-L. Wang, Z.-Q. Ji, Y. Feng, S. Ji, X. Chen, J. Jia, X. Dai, Z. Fang, S.-C. Zhang, K. He, Y. Wang, *et al.*, Experimental observation of the quantum anomalous Hall effect in a magnetic topological insulator, Science **340**, 167 (2013).

[4] C.-Z. Chang, W. Zhao, D. Y. Kim, H. Zhang, B. A. Assaf, D. Heiman, S.-C. Zhang, C. Liu, M. H. W. Chan, and J. S. Moodera, High-precision realization of robust quantum anomalous Hall state in a hard ferromagnetic topological insulator, Nat. Mater. **14**, 473 (2015).

[5] M. Mogi, R. Yoshimi, A. Tsukazaki, K. Yasuda, Y. Kozuka, K. S. Takahashi, M. Kawasaki, and Y. Tokura, Magnetic modulation doping in topological insulators toward higher-temperature quantum anomalous Hall effect, Appl. Phys. Lett. **107**, 182401 (2015).

[6] J. Zhu, Y. Feng, X. Zhou, Y. Wang, H. Yao, Z. Lian, W. Lin, Q. He, Y. Lin, Y. Wang, Y. Wang, S. Yang, H. Li, Y. Wu, C. Liu, J. Wang, J. Shen, J. Zhang, Y. Wang, and Y. Wang, Direct observation of chiral edge current at zero magnetic field in a magnetic topological insulator, Nat. Commun. **16**, 963 (2025).

[7] Y. Deng, Y. Yu, M. Z. Shi, Z. Guo, Z. Xu, J. Wang, X. H. Chen, and Y. Zhang, Quantum anomalous Hall effect in intrinsic magnetic topological insulator $MnBi_2Te_4$, Science **367**, 895 (2020).

[8] C. Liu, Y. Wang, H. Li, Y. Wu, Y. Li, J. Li, K. He, Y. Xu, J. Zhang, and Y. Wang, Robust axion insulator and Chern insulator phases in a two-dimensional antiferromagnetic topological insulator, Nat. Mater. **19**, 522 (2020).

[9] T. Li, S. Jiang, B. Shen, Y. Zhang, L. Li, Z. Tao, T. Devakul, K. Watanabe, T. Taniguchi, L. Fu, J. Shan, and K. F. Mak, Quantum anomalous Hall effect from intertwined moiré bands, Nature (London) **600**, 641 (2021).

[10] M. Serlin, C. L. Tschirhart, H. Polshyn, Y. Zhang, J. Zhu, K. Watanabe, T. Taniguchi, L. Balents, and A. F. Young, Intrinsic quantized anomalous Hall effect in a moiré heterostructure, Science **367**, 900 (2020).

[11] V. Baltz, A. Manchon, M. Tsoi, T. Moriyama, T. Ono, and Y. Tserkovnyak, Antiferromagnetic spintronics, Rev. Mod. Phys. **90**, 015005 (2018).

[12] M. Hafez-Torbati, D. Bossini, F. B. Anders, and G. S. Uhrig, Magnetic blue shift of Mott gaps enhanced by double exchange, Phys. Rev. Res. **3**, 043232 (2021).

[13] M. Hafez-Torbati, F. B. Anders, and G. S. Uhrig, Simplified approach to the magnetic blue shift of Mott gaps, Phys. Rev. B **106**, 205117 (2022).

[14] D. Bossini, M. Terschanski, F. Mertens, G. Springholz, A. Bonanni, G. S. Uhrig, and M. Cinchetti, Exchange-mediated magnetic blue-shift of the band-gap energy in the antiferromagnetic semiconductor MnTe, New J. Phys. **22**, 083029 (2020).

[15] G. Sangiovanni, A. Toschi, E. Koch, K. Held, M. Capone, C. Castellani, O. Gunnarsson, S.-K. Mo, J. W. Allen, H.-D. Kim, A. Sekiyama, A. Yamasaki, S. Suga, and P. Metcalf, Static versus dynamical mean-field theory of Mott antiferromagnets, Phys. Rev. B **73**, 205121 (2006).

[16] Y.-J. Hao, P. Liu, Y. Feng, X.-M. Ma, E. F. Schwier, M. Arita, S. Kumar, C. Hu, R. Lu, M. Zeng, Y. Wang, Z. Hao, H.-Y. Sun, K. Zhang, J. Mei, N. Ni, L. Wu, K. Shimada, C. Chen, Q. Liu, *et al.*, Gapless surface Dirac cone in antiferromagnetic topological insulator $MnBi_2Te_4$, Phys. Rev. X **9**, 041038 (2019).

[17] Y. J. Chen, L. X. Xu, J. H. Li, Y. W. Li, H. Y. Wang, C. F. Zhang, H. Li, Y. Wu, A. J. Liang, C. Chen, S. W. Jung, C. Cacho, Y. H. Mao, S. Liu, M. X. Wang, Y. F. Guo, Y. Xu, Z. K. Liu, L. X. Yang, and Y. L. Chen, Topological electronic structure and its temperature evolution in antiferromagnetic topological insulator $MnBi_2Te_4$, Phys. Rev. X **9**, 041040 (2019).

[18] H. Li, S.-Y. Gao, S.-F. Duan, Y.-F. Xu, K.-J. Zhu, S.-J. Tian, J.-C. Gao, W.-H. Fan, Z.-C. Rao, J.-R. Huang, J.-J. Li, D.-Y. Yan, Z.-T. Liu, W.-L. Liu, Y.-B. Huang, Y.-L. Li, Y. Liu, G.-B. Zhang, P. Zhang, T. Kondo, *et al.*, Dirac surface states in intrinsic magnetic topological insulators $EuSn_2As_2$ and $MnBi_{2n}Te_{3n+1}$, Phys. Rev. X **9**, 041039 (2019).

[19] P. Swatek, Y. Wu, L.-L. Wang, K. Lee, B. Schrunk, J. Yan, and A. Kaminski, Gapless Dirac surface states in the antiferromagnetic topological insulator $MnBi_2Te_4$, Phys. Rev. B **101**, 161109(R) (2020).

[20] K. Jiang, S. Zhou, X. Dai, and Z. Wang, Antiferromagnetic Chern insulators in noncentrosymmetric systems, Phys. Rev. Lett. **120**, 157205 (2018).

[21] M. Ebrahimkhas, G. S. Uhrig, W. Hofstetter, and M. Hafez-Torbati, Antiferromagnetic Chern insulator in centrosymmetric systems, Phys. Rev. B **106**, 205107 (2022).

[22] P.-J. Guo, Z.-X. Liu, and Z.-Y. Lu, Quantum anomalous Hall effect in collinear antiferromagnetism, npj Comput. Mater. **9**, 70 (2023).

[23] M. Hafez-Torbati, Antiferromagnetic topological insulators in heavy-fermion systems, Phys. Rev. B **110**, 115147 (2024).

[24] M. Hafez-Torbati and G. S. Uhrig, Antiferromagnetic Chern insulator with large charge gap in heavy transition-metal compounds, Sci. Rep. **14**, 17168 (2024).

[25] B. Wu, Y.-L. Song, W.-X. Ji, P.-J. Wang, S.-F. Zhang, and C.-W. Zhang, Quantum anomalous Hall effect in an antiferromagnetic monolayer of MoO, Phys. Rev. B **107**, 214419 (2023).

[26] P. Fazekas, *Lecture Notes on Electron Correlation and Magnetism*, Series in Modern Condensed Matter Physics (World Scientific, Singapore, 1999).

[27] See Supplemental Material at http://link.aps.org/supplemental/10.1103/nmxv-m2wf for the DMFT solution of Eq. (2), for a discussion of the ionicity, for the analysis of the Hall conductance in Eq. (3), for the mean-field Néel temperature of the effective spin model, for the calculation of the spectral function on the cylindrical geometry, and for further details of the phase diagram in Fig. 2, which includes Refs. [28,29].

[28] Z. Wang and S.-C. Zhang, Simplified topological invariants for interacting insulators, Phys. Rev. X **2**, 031008 (2012).

[29] B. Hawashin, J. Sirker, and G. S. Uhrig, Topological properties of single-particle states decaying into a continuum due to interaction, Phys. Rev. Res. **6**, L042041 (2024).

[30] C. L. Kane and E. J. Mele, Quantum spin Hall effect in graphene, Phys. Rev. Lett. **95**, 226801 (2005).

[31] A. Georges, G. Kotliar, W. Krauth, and M. J. Rozenberg, Dynamical mean-field theory of strongly correlated fermion systems and the limit of infinite dimensions, Rev. Mod. Phys. **68**, 13 (1996).

[32] M. Caffarel and W. Krauth, Exact diagonalization approach to correlated fermions in infinite dimensions: Mott transition and superconductivity, Phys. Rev. Lett. **72**, 1545 (1994).

[33] M. Potthoff and W. Nolting, Surface metal-insulator transition in the Hubbard model, Phys. Rev. B **59**, 2549 (1999).

[34] Y. Song, R. Wortis, and W. A. Atkinson, Dynamical mean-field study of the two-dimensional disordered Hubbard model, Phys. Rev. B **77**, 054202 (2008).

[35] M. Snoek, I. Titvinidze, C. Tőke, K. Byczuk, and W. Hofstetter, Antiferromagnetic order of strongly interacting fermions in a trap: Real-space dynamical mean-field analysis, New J. Phys. **10**, 093008 (2008).

[36] M. Hafez-Torbati and W. Hofstetter, Artificial SU(3) spin-orbit coupling and exotic Mott insulators, Phys. Rev. B **98**, 245131 (2018).

[37] E. Möller-Hartmann, Correlated fermions on a lattice in high dimensions, Z. Phys. B **74**, 507 (1989).

[38] T. I. Vanhala, T. Siro, L. Liang, M. Troyer, A. Harju, and P. Törmä, Topological phase transitions in the repulsively interacting Haldane-Hubbard model, Phys. Rev. Lett. **116**, 225305 (2016).

[39] T. Mertz, K. Zantout, and R. Valentí, Statistical analysis of the Chern number in the interacting Haldane-Hubbard model, Phys. Rev. B **100**, 125111 (2019).

[40] I. S. Tupitsyn and N. V. Prokof'ev, Phase diagram topology of the Haldane-Hubbard-Coulomb model, Phys. Rev. B **99**, 121113(R) (2019).

[41] W.-X. He, R. Mondaini, H.-G. Luo, X. Wang, and S. Hu, Phase transitions in the Haldane-Hubbard model, Phys. Rev. B **109**, 035126 (2024).

[42] M. Hafez-Torbati, From explicit to spontaneous charge order and the fate of the antiferromagnetic quantum Hall state, Phys. Rev. B **111**, 125108 (2025).

[43] K. Ishikawa and T. Matsuyama, A microscopic theory of the quantum Hall effect, Nucl. Phys. B **280**, 523 (1987).

[44] T. Yoshida, S. Fujimoto, and N. Kawakami, Correlation effects on a topological insulator at finite temperatures, Phys. Rev. B **85**, 125113 (2012).

[45] B. Irsigler, T. Grass, J.-H. Zheng, M. Barbier, and W. Hofstetter, Topological Mott transition in a Weyl-Hubbard model: Dynamical mean-field theory study, Phys. Rev. B **103**, 125132 (2021).

[46] E. Manousakis, The spin-$\frac{1}{2}$ Heisenberg antiferromanget on a square lattice and its application to the cuprous oxides, Rev. Mod. Phys. **63**, 1 (1991).

[47] G. Rohringer, H. Hafermann, A. Toschi, A. A. Katanin, A. E. Antipov, M. I. Katsnelson, A. I. Lichtenstein, A. N. Rubtsov, and K. Held, Diagrammatic routes to nonlocal correlations beyond dynamical mean field theory, Rev. Mod. Phys. **90**, 025003 (2018).

[48] J. H. Van Vleck, *The Theory of Electric and Magnetic Susceptibilities* (Oxford University Press, New York, 1932).

[49] A. Garg, H. R. Krishnamurthy, and M. Randeria, Can correlations drive a band insulator metallic? Phys. Rev. Lett. **97**, 046403 (2006).

[50] N. Paris, K. Bouadim, F. Hébert, G. G. Batrouni, and R. T. Scalettar, Quantum Monte Carlo study of an interaction-driven band-insulator-to-metal transition, Phys. Rev. Lett. **98**, 046403 (2007).

[51] K. Byczuk, M. Sekania, W. Hofstetter, and A. P. Kampf, Insulating behavior with spin and charge order in the ionic Hubbard model, Phys. Rev. B **79**, 121103(R) (2009).

[52] S. S. Kancharla and E. Dagotto, Correlated insulated phase suggests bond order between band and Mott insulators in two dimensions, Phys. Rev. Lett. **98**, 016402 (2007).

[53] M. Hafez-Torbati and G. S. Uhrig, Orientational bond and Néel order in the two-dimensional ionic Hubbard model, Phys. Rev. B **93**, 195128 (2016).

[54] D. I. Khomskii and S. V. Streltsov, Orbital effects in solids: Basics, recent progress, and opportunities, Chem. Rev. **121**, 2992 (2021).

[55] C.-C. Liu, H. Jiang, and Y. Yao, Low-energy effective Hamiltonian involving spin-orbit coupling in silicene and two-dimensional germanium and tin, Phys. Rev. B **84**, 195430 (2011).

[56] Z. Ni, Q. Liu, K. Tang, J. Zheng, J. Zhou, R. Qin, Z. Gao, D. Yu, and J. Lu, Tunable band gap in silicene and germanene, Nano Lett. **12**, 113 (2012).

[57] Y. Zhang, T.-T. Tang, C. Girit, Z. Hao, M. C. Martin, A. Zettl, M. F. Crommie, Y. R. Shen, and F. Wang, Direct observation of a widely tunable bandgap in bilayer graphene, Nature (London) **459**, 820 (2009).

[58] K. Sakanashi, N. Wada, K. Murase, K. Oto, G.-H. Kim, K. Watanabe, T. Taniguchi, J. P. Bird, D. K. Ferry, and N. Aoki, Valley polarized conductance quantization in bilayer graphene narrow quantum point contact, Appl. Phys. Lett. **118**, 263102 (2021).

[59] S. Asai, M. Soda, K. Kasatani, T. Ono, M. Avdeev, and T. Masuda, Magnetic ordering of the buckled honeycomb lattice antiferromagnet Ba_2NiTeO_6, Phys. Rev. B **93**, 024412 (2016).

[60] S. Asai, M. Soda, K. Kasatani, T. Ono, V. O. Garlea, B. Winn, and T. Masuda, Spin dynamics in the stripe-ordered buckled honeycomb lattice antiferromagnet Ba_2NiTeO_6, Phys. Rev. B **96**, 104414 (2017).

[61] G. S. Thakur, T. C. Hansen, W. Schnelle, S. Guo, O. Janson, J. van den Brink, C. Felser, and M. Jansen, Buckled honeycomb lattice compound $Sr_3CaOs_2O_9$ exhibiting antiferromagnetism above room temperature, Chem. Mater. **34**, 4741 (2022).

[62] D. Xiao, W. Zhu, Y. Ran, N. Nagaosa, and S. Okamoto, Interface engineering of quantum Hall effects in digital transition metal oxide heterostructures, Nat. Commun. **2**, 596 (2011).

[63] Q.-F. Liang, L.-H. Wu, and X. Hu, Electrically tunable topological state in [111] perovskite materials with an antiferromagnetic exchange field, New J. Phys. **15**, 063031 (2013).